RESEARCH ARTICLE

Key Points:
- New methodology to estimate geoelectric fields using 3-D magnetotelluric impedance is developed and validated
- Estimates capture 85–90% of the signal for measured geoelectric storm time data in Japan
- Method can be efficiently applied to "nowcast" local geoelectric fields with a tradeoff between accuracy and a modest prediction delay

Correspondence to:
A. Kelbert,
akelbert@usgs.gov

Methodology for time-domain estimation of storm time geoelectric fields using the 3-D magnetotelluric response tensors

Anna Kelbert[1,2] ⓘ , Christopher C. Balch[3] ⓘ , Antti Pulkkinen[4] ⓘ , Gary D. Egbert[2], Jeffrey J. Love[1] ⓘ , E. Joshua Rigler[1] ⓘ , and Ikuko Fujii[5] ⓘ

[1]Geomagnetism Program, U.S. Geological Survey, Denver, Colorado, USA, [2]College of Earth, Ocean and Atmospheric Sciences, Oregon State University, Corvallis, Oregon, USA, [3]NOAA Space Weather Prediction Center, Boulder, Colorado, USA, [4]NASA Goddard Space Flight Center, Greenbelt, Maryland, USA, [5]Meteorological College, Kashiwa, Japan

Abstract Geoelectric fields at the Earth's surface caused by magnetic storms constitute a hazard to the operation of electric power grids and related infrastructure. The ability to estimate these geoelectric fields in close to real time and provide local predictions would better equip the industry to mitigate negative impacts on their operations. Here we report progress toward this goal: development of robust algorithms that convolve a magnetic storm time series with a frequency domain impedance for a realistic three-dimensional (3-D) Earth, to estimate the local, storm time geoelectric field. Both frequency domain and time domain approaches are presented and validated against storm time geoelectric field data measured in Japan. The methods are then compared in the context of a real-time application.

Plain Language Summary Magnetic storms can pose significant risks to critical technology infrastructure such as the electric power grids. Real-time estimation of geoelectric fields can give the grid operators an opportunity for prompt intervention that would mitigate the long-term consequences. We develop and validate a method to efficiently and accurately (to within 85–90%) "nowcast" storm time geoelectric fields in close to real time in places where both geomagnetic field data are collected or estimated, and a magnetotelluric impedance has been previously measured. This method can be applied in all regions where magnetotelluric data have been collected, including in the United States, where USArray magnetotelluric data survey is ongoing and by 2018 will cover about two thirds of the country. In this work, we focus on the algorithm development only.

1. Introduction

Magnetic storms can induce geoelectric fields in the Earth's electrically conducting interior, interfering with the operation of electric power grids and pipelines [e.g., *Albertson et al.*, 1993; *Boteler*, 2003; *Samuelsson*, 2013; *Piccinelli and Krausmann*, 2014]. The potential risks were dramatically demonstrated during the magnetic storm of March 1989 [e.g., *Allen et al.*, 1989], which caused strong geomagnetically induced currents (GICs) to flow along the power lines, collapsing the entire Hydro-Québec electric power grid in Canada [*Bolduc*, 2002; *Béland and Small*, 2005], as well as causing severe damage to step-up transformers in Delaware Bay (see *North American Electric Reliability Corporation (NERC)* [1990], for a compilation of effects). However, in all likelihood, humanity's technological age has not yet lasted long enough to experience the solar activity to its full potential. Under some scenarios, the future occurrence of a rare but extremely intense magnetic superstorm could well cause a similar or more severe cascading failure in power transmission, resulting in a widespread blackout that would cause significant harm to our society's economy and well-being [*Baker et al.*, 2008; *NERC*, 2012]. Significant hazards that solar activity poses to our modern day infrastructure have motivated regulatory agencies to require utility companies to take measures to mitigate the potential impact of geomagnetic disturbances on the operation of bulk-electric power systems [*Federal Energy Regulatory Commission (FERC)*, 2013, Order No. 779; *FERC*, 2016, Order No. 830], and the significance of the hazard is also recognized at the U.S. National Strategic level [e.g., *National Science and Technology Council*, 2015, Goals 1.1 and 5.5].

Accurate calculation of geoelectric fields, ideally in close to real time, is an important goal for studies concerned with induction hazard monitoring and assessment [e.g., *Thomson et al.*, 2009; *Love et al.*, 2014; *Pulkkinen et al.*, 2017]. A focused effort by the U.S. government agencies to provide an electric field nowcasting capability to the public was originally motivated by the industry consensus at the NOAA Space Weather Workshop 2011. Indeed, a high-resolution regional nowcast is a more precise indicator of induction than *Kp* index (a mean standardized 3 h index measure from 13 geomagnetic observatories between 44° and 60° northern or southern geomagnetic latitude). Incorporated into daily industrial workflow, nowcasting could improve situational awareness and allow for more targeted and therefore less economically damaging action. It would also provide a key stepping stone toward a prediction and mitigation workflow.

Such calculations convolve a time series of geomagnetic field data, streaming in real time, with a surface impedance tensor that is, itself, a function of the subsurface electrical conductivity structure. Calculation of synthetic storm time geoelectric fields have been performed for many geographic regions [e.g., *Boteler*, 2001; *Gannon et al.*, 2012, 2013; *Viljanen et al.*, 2013; *Wei et al.*, 2013; *Marti et al.*, 2014b] and used in scenario simulations of geomagnetically induced currents in power grids [e.g., *Pulkkinen et al.*, 2012; *Viljanen et al.*, 2013; *Torta et al.*, 2014]. These calculations have used Earth impedances derived under the assumption that local stratigraphy, tectonic structure, and rock properties can be reasonably modeled as a one-dimensional (1-D) function of depth [e.g., *Ferguson and Odwar*, 1997; *Fernberg*, 2012]. Other analyses have demonstrated that 3-D Earth structure can have a significant effect on the local amplitude, polarization, and phase of geoelectric fields [e.g., *McKay et al.*, 2006; *Bedrosian and Love*, 2015]. For example, *Bedrosian and Love* [2015] showed that the amplitude of geoelectric fields can differ by an order of magnitude between two locations 70 km apart due to a 2–3 orders of magnitude variation in Earth's conductivity often observed for North American lithosphere. A recent publication by *Weigel* [2017] performed a comparative analysis of estimated quiet time geoelectric fields that further illustrated the limitations of using the 1-D approximation, compared to realistic 3-D Earth impedances, for geoelectric field estimation. Another recent work by *Bonner and Schultz* [2017] has put forward a procedure to interpolate sparse observatory geomagnetic fields to an arbitrary site location and use the 3-D Earth impedances to estimate surface geoelectric fields using a frequency domain algorithm. *Bonner and Schultz* [2017] validated their method using a quiet time USArray time series [*Schultz et al.*, 2006-2018] and compared the results with those using a 1-D approximation of the Earth. They confirmed that 3-D Earth impedances result in significantly better estimates of geoelectric fields compared to those obtained from 1-D electrical conductivity profiles. We revisit this issue in the appendices of this manuscript, where we consider the applicability of a 1-D method to geoelectric field estimation in Japan and justify our choice to work with a 3-D Earth impedance. We note, however, that empirical or modeled 3-D Earth impedances are accurate at the precise location where they are obtained. In this sense, 3-D Earth impedances and the estimated geoelectric fields are local and cannot be used in a regional sense. For GIC computations, local geoelectric field estimates would need to be integrated along a power line, which amounts to an averaging procedure that may, in some places, be comparable to using a regional 1-D impedance. Such a comparison is beyond the scope of this manuscript.

As we further discuss in section 2, the Earth impedance is best represented in the frequency domain. Converting geomagnetic field time series to the frequency domain is also reasonably straightforward, so prior electric field computations have mostly adopted that approach. While a time domain approach, in which the Earth impedance is converted to an impulse response, might have some advantages over frequency domain for real-time natural hazard applications, no comprehensive comparisons of these two formulations have ever been performed. Variants of time-domain approaches have been used in the past for 1-D conductivity models [e.g., *Marti et al.*, 2014a and *Kappenman et al.*, 2000]. In contrast, the current work considers the application of time-domain methods for real-time electric field "nowcasting" using more realistic 3-D Earth impedances. As compared to, e.g., *Marti et al.* [2014a], our method is uniquely capable of not only using the empirical magnetotelluric (MT) impedances for electric field estimation but also of accounting for their uncertainties: a necessary step to progress to using empirical MT impedances such as those provided by USArray [*Schultz et al.*, 2006-2018] for practical geoelectric field estimation. This has allowed us to validate our technique against measured storm time geoelectric field data and to quantify storm time electric field estimation errors with unprecedented accuracy. We focus on the development and validation of a novel time domain geoelectric field computation algorithm based on *Egbert* [1992] discrete time impulse response (DTIR) technique developed initially for the 1-D impedance. We also provide a side-by-side comparison of our method with the more traditional frequency domain approach to the problem.

We start with an introductory section that provides a high-level overview of the method of magnetotellurics (MT) and defines the magnetotelluric response function (section 2). We then describe the standard frequency domain geoelectric field estimation method (section 3) and introduce the discrete time impulse response technique (section 4). For convenience of the reader, technical details of the time domain algorithm implementation are provided in the appendices. We then compare the time domain method with the frequency domain discrete Fourier transform method and discuss the relative benefits of both approaches while also validating these methods with respect to measured storm time geoelectric field data (section 5). We discuss the goodness of fit and the limitations of using a local response function for geoelectric field estimation in section 6. In section 7, we apply both methods in real time and discuss the additional errors that are involved due to a real-time application of the time domain algorithm, as compared to the errors resulting from a similar application of the frequency domain method. Due to the additional complexity related to a causal algorithm implementation and its validation, a general real-time implementation of this method is outside of the scope of this work and will be explored in detail in a subsequent publication. We conclude our analysis with a summary and suggestions for future work in section 8.

2. Magnetotelluric Response Function

The methods of magnetotellurics (MT) [e.g., *Cagniard*, 1953 and *Chave and Jones*, 2012] are generally concerned with using ground level geomagnetic and geoelectric field measurements to estimate the electrical conductivity of the solid Earth. In magnetotellurics, conductivity models are obtained from a derived data product known as the *magnetotelluric (MT) response tensor* $\mathbf{Z}(f, x, y)$, which is also sometimes referred to as an *MT transfer function*. The MT response tensor is a frequency-dependent relationship between the horizontal components of the geomagnetic field at the Earth's surface and the horizontal components of the ground level geoelectric field:

$$\tilde{\mathbf{E}}_h(f, x, y) = \mathbf{Z}\left(f, x, y\right) \cdot \tilde{\mathbf{B}}_h(f, x, y) \tag{1}$$

[e.g., *Weidelt and Chave*, 2012, Chapter 4.1.2], where the horizontal geomagnetic $\mathbf{B}_h(t)$ and geoelectric $\mathbf{E}_h(t)$ time series have been Fourier transformed into a frequency domain representation at a discrete set of frequencies, (x, y) is Earth's surface location and f is frequency. At each discrete frequency f and location (x, y), $\mathbf{Z}$ is a 2×2 complex-valued matrix and is related to the *MT impedance* $\mu\mathbf{Z}$ (measured in ohms), where μ is the magnetic permeability via a simple rescaling of units. To avoid potential confusion caused by the multiple unit conventions used to describe the MT impedance, throughout this manuscript we employ the term "MT response" for $\mathbf{Z}$ and use the following practical units: $\mathbf{B}$ is measured in nT, $\mathbf{E}$ in mV/km, and the MT response tensor has the units of (mV/km)/nT, a convention that is commonly accepted within academia and industry.

Equation (1) can be simplified for certain idealized Earth conductivity structures. For a half-space of uniform conductivity, the MT response is proportional to the square root of the inductional frequency f, and the time-varying sinusoidal amplitude of the geoelectric field leads that of the geomagnetic field by a phase of $\pi/4$ (or 45°). For an idealized Earth conductivity that varies only with depth (1-D) [e.g., *Simpson and Bahr*, 2005, Chapter 2.5], the response tensor is antisymmetric,

$$\mathbf{Z}\left(f\right) = \begin{bmatrix} 0 & Z \\ -Z & 0 \end{bmatrix}(f) \quad \text{(1-D),} \tag{2}$$

where each nonzero element Z is complex-valued and frequency-dependent. For an idealized 1-D response, geomagnetic activity $\mathbf{B}_h(t_i)$ aligned in a given horizontal direction will induce an orthogonal geoelectric field $\mathbf{E}_h(t_i)$, so that $\mathbf{E}_h \cdot \mathbf{B}_h = 0$. In the presence of a clear geoelectric strike such that the Earth conductivity varies with depth and in one lateral direction, a two-dimensional (2-D) approximation may be appropriate,

$$\mathbf{Z}\left(f, x, y\right) = \begin{bmatrix} 0 & Z_{xy} \\ Z_{yx} & 0 \end{bmatrix}(f, x, y) \quad \text{(2-D),} \tag{3}$$

where only the off-diagonal components of MT response take nonzero values, such that $E_x = Z_{xy}B_y$ and $E_y = Z_{yx}B_x$, with the fields rotated to point along and perpendicular to geoelectric strike.

In general, none of these simple functional relationships are observed in empirical response tensors [e.g., *Schultz et al.*, 2006-2018] which are generally fully populated and asymmetric [e.g., *Chave*, 2012],

$$\mathbf{Z}\left(f,x,y\right) = \begin{bmatrix} Z_{xx} & Z_{xy} \\ Z_{yx} & Z_{yy} \end{bmatrix} \left(f,x,y\right) \quad \text{(3-D)}, \tag{4}$$

where each response tensor element, for example, Z_{xx}, has no simple mathematical relationship to the other response tensor elements, Z_{xy}, Z_{yx}, and Z_{yy}.

Traditionally, magnetotelluric methods have allowed for 1-D or 2-D interpretations in terms of the Earth conductivity, using the simplified versions of the MT responses appropriate for these special cases (equations (2) and (3), respectively). The past decade, however, has seen the advent of 3-D magnetotellurics, which allows estimation of electrical conductivity structure within a 3-D Earth volume with reasonably high resolution that is commensurate with station spacing, and ranges from hundreds of meters for local studies to tens of kilometers on continental scales.

Magnetotelluric inversion is a computationally intensive, nonlinear and nonunique inverse problem [e.g., *Siripunvaraporn et al.*, 2005; *Egbert and Kelbert*, 2012]. Thus, there could be a variety of 3-D models that fit the measured MT responses to within their estimated precision. A phenomenon known as *galvanic distortion*, which refers to small-scale, local structures obscuring the regional signal in the data, is also a problem [e.g., *Groom and Bailey*, 1989]. However, large-scale 3-D MT inversions of recent years [e.g., *Meqbel et al.*, 2014; *Bedrosian and Feucht*, 2014; *Yang et al.*, 2015] have demonstrated significant correlations with independently observed geological structures. Three-dimensional MT responses can be either empirical, i.e., estimated from measured data, or computed from a 3-D electrical conductivity model obtained by inverting the empirical responses. Here we explore storm time prediction efficiency of empirical 3-D MT responses obtained from measured geomagnetic and geoelectric field data (section 5).

A historical approach to estimation of the MT response [e.g., *Sims et al.*, 1971] is to Fourier transform the magnetic and electric field time series directly and to solve equation (1) for the MT response via a least squares procedure. The simple direct (unweighted) least squares approach relies on the assumptions that the error variances are independent of signal power and that the errors are Gaussian and uncorrelated. In MT applications, these assumptions have been repeatedly shown to fail in the presence of outliers or significant source effects, such as during a magnetic storm (see, e.g., *Egbert and Booker* [1986] for a thorough analysis of this issue). Instead, a variety of data adaptive robust estimation schemes for MT responses have been developed over the years (most notably, *Egbert and Booker* [1986], *Chave et al.* [1987], *Smirnov and Egbert* [2012], and *Chave* [2014]. These techniques employ variants of least squares method that are resistant to violations of distributional assumptions, leverage points, and outliers. Robust estimates produce an MT response tensor that does not vary depending on the segment of the time series that is used for the estimate, except within the error bars, thus reducing the dependence of the MT response on the ionospheric and other nonperiodic (e.g., cultural) source effects.

By design, the robust MT response estimates are affected less by inclusion of storm time data than the simple direct least squares approach. Except in the presence of periodic cultural, tidal, or temperature effects, or at high latitudes where a non-plane wave signal could dominate during a magnetic storm, a robust MT response is a function of the Earth conductivity and will not vary whether obtained using storm time data or during a quiet time. The enhanced signal-to-noise ratio observed during a magnetic storm does allow better constraint of the error bars, but this signal is otherwise downweighted in the robust estimation procedure. Indeed, the basic assumption of the MT method is a plane wave structure of the ionospheric source: an approximation that may well fail during a severe storm, especially at higher geomagnetic latitudes. This has led some to reconsider the need for robust estimation in application to the GIC prediction problem. For instance, *Weigel* [2017] demonstrates that under certain circumstances (such as an unusually clean time series segment), the simple direct least squares technique allows for a slightly better estimate of the geoelectric field. However, it should be noted that in the examples that were considered by *Weigel* [2017], the adjacent in-sample and out-of-sample time series segments were likely affected by the same or very similar ionospheric source configurations. As all storms are distinct from one another, it is an open question whether these estimates would still do a reasonable job at estimating the geoelectric fields at a different time. Another word of warning is that clean and unbiased electric time series are an extremely rare occurrence and it often takes an expert to

identify noise and bias. Careful preprocessing of the time series is needed to minimize the effects of noise and bias during robust MT response estimation and especially so for simple direct least squares.

Finally, the components of the MT response tensor at frequency f are often represented as so-called apparent resistivity ρ_{ij} and phase ϕ_{ij} [*Vozoff*, 1972]:

$$\rho_{ij}(f) = \frac{|\mathbf{Z}_{ij}(f)|^2}{5f} \tag{5}$$

$$\phi_{ij}(f) = \arctan\left[\frac{\text{Im } \mathbf{Z}_{ij}(f)}{\text{Re } \mathbf{Z}_{ij}(f)}\right] \tag{6}$$

where subscript ij stands for the response tensor components xx, xy, yx, and yy. Typically, only the two off-diagonal components are plotted for interpretation on apparent resistivity and phase plots of the MT response. This is because the phases are not well-defined as the diagonal impedance components approach zero, as is observed for near 1-D conductivities. Apparent resistivity has the units of Ohm m and has direct physical interpretation for simple Earth models such as a uniform half-space. In section 5, we plot apparent resistivities and phases along with the full MT response, as a function of period.

3. Frequency Domain Geoelectric Field Estimation

As is evident from section 2, estimation of geoelectric fields at the Earth's surface is not a traditional goal for the science of magnetotellurics. It does however come naturally as a byproduct of the well-developed MT tools. In the United States, for example, many robust MT response tensors are now available at the database of *Kelbert et al.* [2011], with more MT data being collected and processed daily by the NSF's USArray MT program [*Schultz et al.*, 2006-2018] and many other initiatives. These data can be reused, in conjunction with continuous geomagnetic field measurements [e.g., *Love and Finn*, 2011; *Lam*, 2011], to estimate surface geoelectric fields in close to real time.

The frequency domain method for estimating the electric field time series begins by carrying out a discrete Fourier transform (DFT) of the horizontal components of geomagnetic field time series $\mathbf{B}_h(\mathbf{t})$ to derive the frequency domain components $\tilde{\mathbf{B}}_h(\mathbf{f})$. Formally, for a time series with N discrete samples collected over a finite interval of $N * \delta t$ seconds, at times $t_k = k * \delta t$, $k = 0, 1, 2, \ldots, N - 1$, the N-point DFT is obtained by

$$\tilde{\mathbf{B}}_h(f_m) = \sum_{k=0}^{N-1} \mathbf{B}_h(t_k) \exp\left(-i2\pi f_m t_k\right)\delta t, \quad \text{for} \ \ m = 0, 1, 2, \ldots, N - 1. \tag{7}$$

where $f_m = m/(N\delta t)$, which defines $\delta f = 1/(N\delta t)$ as the frequency resolution of $\tilde{\mathbf{B}}_h(\mathbf{f}_m)$. (Here we follow the notation recommendations of *Boteler* [2012]).

We note that the exponent $2\pi f_m t_k = 2\pi m\delta f k\delta t = 2\pi mk/N$, so the functions $\exp\left(-i2\pi f_m t_k\right) = \exp\left(-i2\pi mk/N\right)$ are periodic in time on the interval $[0, T)$ and are also periodic in frequency on the interval $[0, Ndf)$, for $m = 0, 1, 2, \ldots, N - 1$ and for $k = 0, 1, 2, \ldots, N - 1$, i.e., $\exp\left(-i2\pi f_m t_k\right) = \exp\left(-i2\pi f_{m+N} t_k\right) = \exp\left(-i2\pi f_m t_{k+N}\right)$.

The next step is to infer the MT response tensor at the discrete frequencies $f_m = m\delta f$, which typically involves interpolation and resampling. We do the resampling for all the frequencies from 0 up to the Nyquist frequency $(N/2) \times \delta f$. For real-valued time series such as the $\mathbf{B}_h(t_k)$, the frequencies with $m > N/2$ are conjugates of frequencies at negative indices $(m - N)$. For each such conjugate frequency, there is a corresponding positive frequency index $(N - m)$, and it can be shown that since both $\mathbf{B}_h(t_k)$ and $\mathbf{E}_h(t_k)$ are real-valued functions, the MT response at a negative frequency is the complex conjugate of the MT response at the corresponding positive frequency.

Having obtained $\tilde{\mathbf{B}}_h(\mathbf{f})$ and resampled the discrete MT response to the same set of frequencies $\mathbf{f}$, we can apply equation (1) to obtain the geoelectric field in the frequency domain, $\tilde{\mathbf{E}}_h(\mathbf{f})$. The final step in the calculation is the application of the inverse discrete Fourier transform (IDFT) to obtain the geoelectric field time series,

$$\mathbf{E}_h(t_k) = \sum_{m=0}^{N-1} \exp\left(i2\pi f_m t_k\right)\tilde{\mathbf{E}}_h(f_m)\delta f, \quad \text{for} \ \ k = 0, 1, 2, \ldots, N - 1. \tag{8}$$

We should explicitly note that in this analysis, there is no provision at present to take the error bars in the MT responses into account when the geoelectric fields are computed. Our goal here is to provide a relatively straightforward baseline algorithm to serve as a benchmark comparison for the more involved time-domain method developed in section 4.

We note that the calculated geoelectric field $\mathbf{E}_h(\mathbf{t})$ is a linear superposition of periodic functions on the interval $[0, T]$, which necessarily means that $\mathbf{E}_h(\mathbf{t})$ is also periodic on $[0, T]$. In practice, for a given sample of observations $\mathbf{B}_h(\mathbf{t})$ there often will be a significant difference between $\mathbf{B}(0)$ and $\mathbf{B}(t_{N-1})$. The DFT analysis presumes that $\mathbf{B}_h(\mathbf{t})$ is periodic, implying that the point $\mathbf{B}(t_N) = \mathbf{B}(0)$. Typically, then, the DFT sees a step function in the time series from t_{N-1} to t_N, which will add unphysical spectral power at the higher frequencies in $\tilde{\mathbf{B}}_h(\mathbf{f})$. This can be mitigated by applying a Parzen window to an extended geomagnetic field time series [see, e.g., *Viljanen et al.*, 2006], or by "padding" the start and end of the time series by a certain number of points. For the demonstration presented in this paper, we have chosen to use 83 min of padding or 5000 points for 1 s data, which we found to be optimal for our purposes. Rather than padding with zero values as would be more standard but introduces a step function just before t_0 and just after t_{N-1}, we pad by repeating the first and the last values in the time series for the chosen number of minutes — a strategy that we observed to work well, validated by practical tests with multiple MT responses.

4. Discrete Time Domain Geoelectric Field Estimation

The geoelectric fields at the Earth's surface exhibit nontrivial variability in both space and time. The process of electromagnetic induction in a (essentially time stationary) 3-D Earth causes the geoelectric fields to vary from one location to another; however, the time variations in the geoelectric fields are caused by transient and nonstationary magnetic disturbances. These field characteristics are reflected in the geomagnetic field measurements that come as a discrete time series at a certain sampling rate (these days, usually at 1 s intervals) [e.g., *Love and Chulliat*, 2013]. While the frequency domain approach of section 3 allows one to obtain reasonably accurate geoelectric field estimates using empirical MT response tensors [e.g., *Weigel*, 2017; *Bonner and Schultz*, 2017], it is of interest to also explore time domain approaches that may be better suited for treating transient signals. We therefore consider an alternative approach that presents geoelectric field prediction as a discrete time domain problem. We proceed to describe the methodology here and will revisit its real-time application in section 7.

By the convolution theorem [e.g., *Bracewell*, 2000, Chapter 3], the continuous time-domain expression of (1) is given by the integral

$$\mathbf{E}_h(t) = \hat{\mathbf{Z}} * \mathbf{B}_h(t) = \int_{-\infty}^{+\infty} \hat{\mathbf{Z}}(\theta)\mathbf{B}_h(t - \theta)\mathrm{d}\theta. \tag{9}$$

In certain conditions such as the 1-D Earth, this equation is strictly causal [e.g., *Weidelt*, 1972, p. 264], so that $\hat{\mathbf{Z}}(t) = 0$ for $t < 0$. But equation (9) is an idealization; most importantly, it assumes $\mathbf{B}_h(t)$ to have infinitesimal time resolution, which is equivalent to no frequency band limit. In practice, $\mathbf{B}$ data are band limited, since they are collected as discrete samples after analog filtering through an acquisition system, as well as over a finite duration of time. In this case, the continuous equation (9) is replaced by the discrete equation approximation

$$\mathbf{E}_h(t_k) = \hat{\mathbf{Z}} * \mathbf{B}_h(t_k) = \sum_{n=N_{t_-}}^{N_{t_+}} \hat{\mathbf{Z}}(t_n)\mathbf{B}_h(t_k - t_n), \tag{10}$$

where the truncation to the time interval $[N_{t_-}, N_{t_+}]$ is implied, $N_{t_-} \leq 0$ and $N_{t_+} > 0$ being integer lengths of time measured in the number of samples in the negative and positive time directions, respectively.

Here $\hat{\mathbf{Z}}(t_k)$ is the discrete time domain impulse response (DTIR) estimate, as defined in *Egbert* [1992]. In contrast with its continuous form in equation (9), equation (10) is acausal [*Egbert*, 1992] even for the simplest 1-D problem that is strictly causal in continuous time. In other words, $\hat{\mathbf{Z}}(t_k) \neq 0$ for $t_k < 0$. This can be understood if we notice that the discrete sampling in the frequency domain can be represented by a set of "boxcar" functions in the continuous frequency domain, where each impedance value is constant over a frequency band, then jumps discontinuously to the following frequency band. The Fourier transform of a boxcar is proportional to a sinc function, $\sin(t)/t$, and this extends over all time (past and future).

In practice, we obtain an estimate of the DTIR by solving equation 11 of *Egbert* [1992] using a regularized least squares approach:

$$\mathbf{Z}(f_m) = \sum_{n=N_{t-}}^{N_{t+}} \hat{\mathbf{Z}}(t_n) \exp\left(-i2\pi f_m t_n\right) + \epsilon_m, \tag{11}$$

with $m = 1, \ldots, N_f$, where N_f is the number of frequencies (equivalently, periods) in the discretely sampled frequency domain MT response estimate, f_m is the nth sampling frequency, and $t_n = n\delta t$, where δt is the sampling rate of the time series, and ϵ_m is the corresponding complex estimation error for the mth response tensor, with variance σ_m^2.

Consider a real-valued vector of MT response tensor components at a single frequency f_m:

$$\mathbf{Z}(f_m) = \begin{bmatrix} \text{Re}[Z_{xx}(f_m)] \; \text{Im}[Z_{xx}(f_m)] \; \text{Re}[Z_{xy}(f_m)] \; \text{Im}[Z_{xy}(f_m)] \ldots \\ \text{Re}[Z_{yx}(f_m)] \; \text{Im}[Z_{yx}(f_m)] \; \text{Re}[Z_{yy}(f_m)] \; \text{Im}[Z_{yy}(f_m)] \end{bmatrix}.$$

In the following, we denote by $\mathbf{z}_f$ the discrete vector of frequency-domain MT responses $\mathbf{Z}(f_m)$ for all frequencies $m = 1, \ldots, N_f$; $\mathbf{z}_f$, then, is of length $8 \times N_f$. The truncated DTIR representation of $\hat{\mathbf{Z}}(t_n)$ for $n = N_{t-}, \ldots, 0, \ldots, N_{t+}$, where $t_n = n * \delta t$, is denoted by the vector $\mathbf{z}_t$. The length of the impulse response vector is thus $N_t = N_{t+} - N_{t-} + 1$. Note that since the DTIR is real and the frequency domain MT response is complex, we solve the system in real space by considering the real and imaginary components of the MT response tensor elements as separate data points.

Then, equation (11) can be expressed as a linear system

$$\mathbf{z}_f = A\mathbf{z}_t + \epsilon, \tag{12}$$

where A is a full real-valued matrix of size $8N_f \times N_t$ that relates the real-valued impulse response to the real-valued MT response components as defined by equation (11).

In this paradigm, it may be appropriate to talk about the *model* being the vector unknown $\mathbf{z}_t$ (DTIR), and of the known $\mathbf{z}_f$, the frequency domain MT response, as the *data*. Then, regularized least squares solution minimizes

$$\phi(\mathbf{z}_t) = (\mathbf{z}_f - A\mathbf{z}_t)^T \Sigma \, (\mathbf{z}_f - A\mathbf{z}_t) + \lambda \mathbf{z}_t^T Q \mathbf{z}_t, \tag{13}$$

where Σ is the data covariance operator that is constructed using the estimated error bars in $\mathbf{z}_f$, the MT response, while the Q matrix and the scalar damping parameter λ jointly determine the regularization term. The regularized least squares solution is then found by solving a discrete linear system,

$$(A^T \Sigma A + \lambda Q)\mathbf{z}_t = A^T \Sigma \mathbf{z}_f. \tag{14}$$

We have implemented this approach with both varieties of Q matrix defined in *Egbert* [1992] and found that the variant which imposes smoothing in the log-frequency space is the regularization of choice that both improves the long-period fits and minimizes artifacts in the DTIR (see Appendix B for details).

5. Validation Against Measured Geoelectric Field Data

High-quality, long-term geoelectric field measurements are notoriously difficult to obtain. The three geomagnetic observatories in Japan, Kakioka (KAK), Kanoya (KNY), and Memambetsu (MMB) have pioneered long-term high-quality geoelectric field data collection: geoelectric field data recordings at these three observatories commenced, respectively, in the years 1932, 1948, and 1949 and are still ongoing. Long-period MT responses have also been estimated for these three locations by *Fujii et al.* [2015] using the robust method of *Chave et al.* [1987]. Because of the long time series that covers several major storms, the quality of the data, and the three-dimensional (3-D) complexity of Japan (in fact, all three sites are in complex coastal areas), this unique data set provides an appealing opportunity for validation of our method. For clarity of presentation, from now on we focus solely on the Memambetsu (MMB) observatory data. Similar results have been obtained at the other two locations.

To apply the DTIR technique to the time series, we first of all invert the MT responses using the linear least squares method of section 4, to obtain a well-fitting DTIR. A truncated snapshot of DTIR is shown in Figure 1. We note that in this rare example, the length and quality of the time series has allowed for estimation
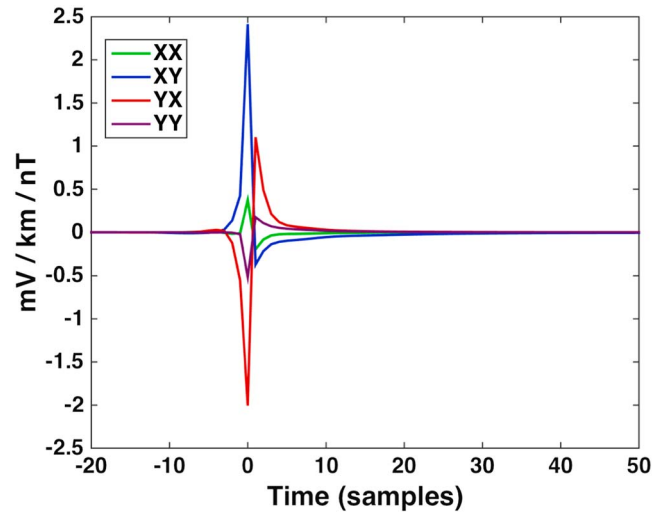
Figure 1. A segment of the discrete time impulse response (DTIR) obtained as a fit to a representative MT response at Memambetsu. The complete DTIR spans the time window from −10 min to +6 h (or [−600 21,600]). We find that a shorter time window is not sufficient to adequately fit the unusually long-period MT response at Memambetsu.

of the MT response at the unprecedented long periods of up to 200,000 s. This gives us a better chance of reproducing the long-period structure of the geoelectric field in our prediction. On the other hand, it comes with its own challenges: an impulse response with a much longer time window is necessary to fit this MT response, than would be typical for, e.g., EarthScope MT responses in the USA which are normally estimated for the periods from 10 to 20,000 s. In fact, the linear smoothing procedure, which is usually sufficient
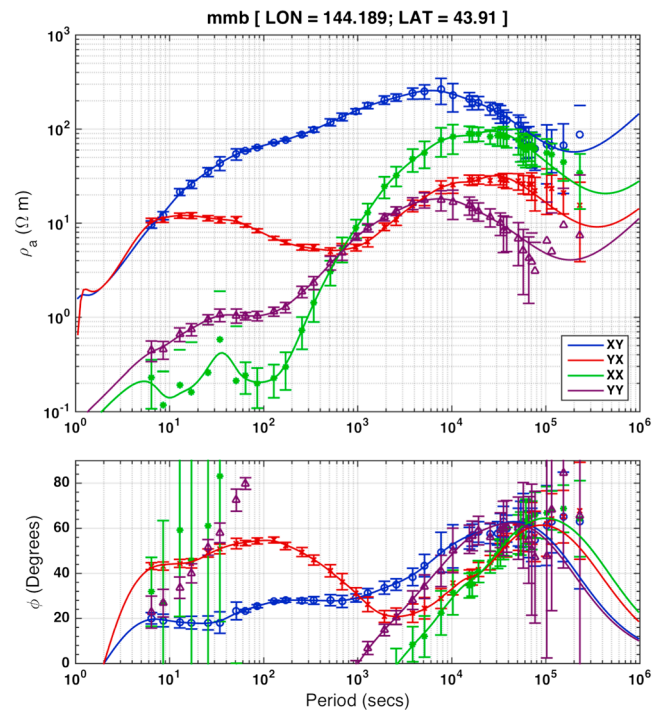

Figure 2. The four components of the empirical 3-D MT response tensor at Memambetsu, plotted as apparent resistivity (ρ) and phase (ϕ), with error bars. In a 1-D Earth, the diagonal components of ρ XY (blue) and YX (red) would coincide, representing the inverse of the electrical conductivity, with period serving as proxy for depth, and the diagonal components XX (green) and YY (purple) would be zero. The fitted lines represent the DTIR prediction. Note that the period range is unusually wide: it is rare for an MT response tensor to extend much beyond 10,000 s.
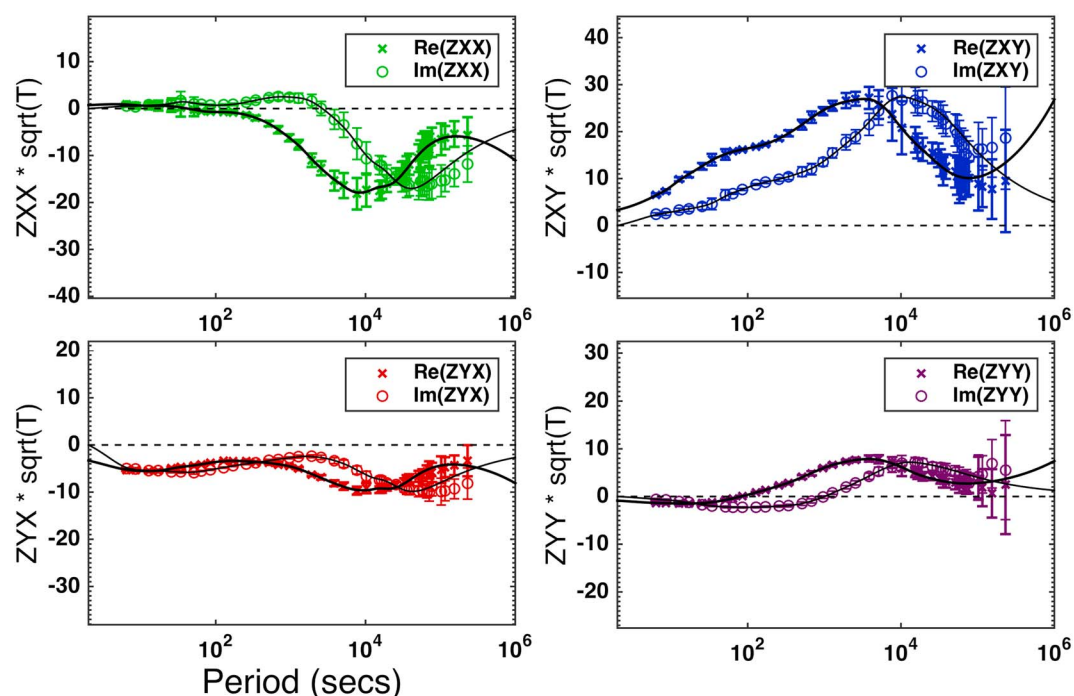
Figure 3. The four components of the empirical 3-D MT response tensor at Memambetsu, traditionally represented as the complex-valued component weighed by the square root of the period T (in seconds), with error bars. The fitted lines are the synthetic MT response predicted by the DTIR.

for EarthScope MT data, no longer produces adequate fits for these long-period responses (see the Appendix B for details, and Appendix C for efficiency considerations). We empirically found that a value of the damping parameter $\lambda = 5e-12$ using the log linear smoothing and a time window that spans from negative $N_{t-} = -600$ to positive $N_{t+} = 21,600$ samples of 1 s time series (i.e., from −10 min to 6 h) allow us to fit the MT response adequately. We used a diagonal data covariance matrix to account for the estimated errors in the MT response. For validation of DTIR, we recompute the MT response $\mathbf{z}_f$ at 300 logarithmically spaced frequencies using equation (12) and compare the results to the measured MT response. The root-mean-square misfit of our DTIR fit to the MT response tensor is 0.53, 0.64, 0.77, and 0.48 for XX, XY, YX, and YY components, respectively. We plot the apparent resistivity and phase at MMB, and their DTIR fits (continuous lines), as well as the full MT response with DTIR fits, in Figures 2 and 3, respectively.

For this analysis, we have chosen the series of "Halloween storms of 2003," at the peak of solar activity of 29–31 October 2003, hereafter referred to as the Halloween storm. This storm is nicely illustrated with a clean geomagnetic and geoelectric field series recording at MMB observatory. At its peak, the Halloween storm of 29–31 October exhibited a series of two intense, $K_p = 9$ durations of disturbance, one closely following the other. In Figure 4, we plot the two components of measured and detrended geomagnetic field **B** in nT for this time period.

We proceed to convolve our DTIR with the measured and detrended geomagnetic field time series, to obtain an estimated electric field time series that could be compared with the measured data. Similarly, we also apply the FFT technique of section 3 to get a second estimated electric field time series. In Figure 5, we plot the two components of **E** in mV/km for a period of 1 day at the onset of the second storm. The time series plotted in blue represents the observed MMB geoelectric field, except that the linear trend is once again taken out before plotting. The estimated geoelectric fields are also plotted in red (FFT) and green (DTIR). It is clear that the waveform of the measured geoelectric field is followed very closely by both estimates.

We now proceed to analyze and quantify the errors in our geoelectric field estimates. For this, we refer the reader to Figure 6. Figure 6 (top left) and 6 (top right) show the three geoelectric field time series plotted on top of one another using the same conventions as in Figure 6 for both geoelectric field components E_x and E_y,
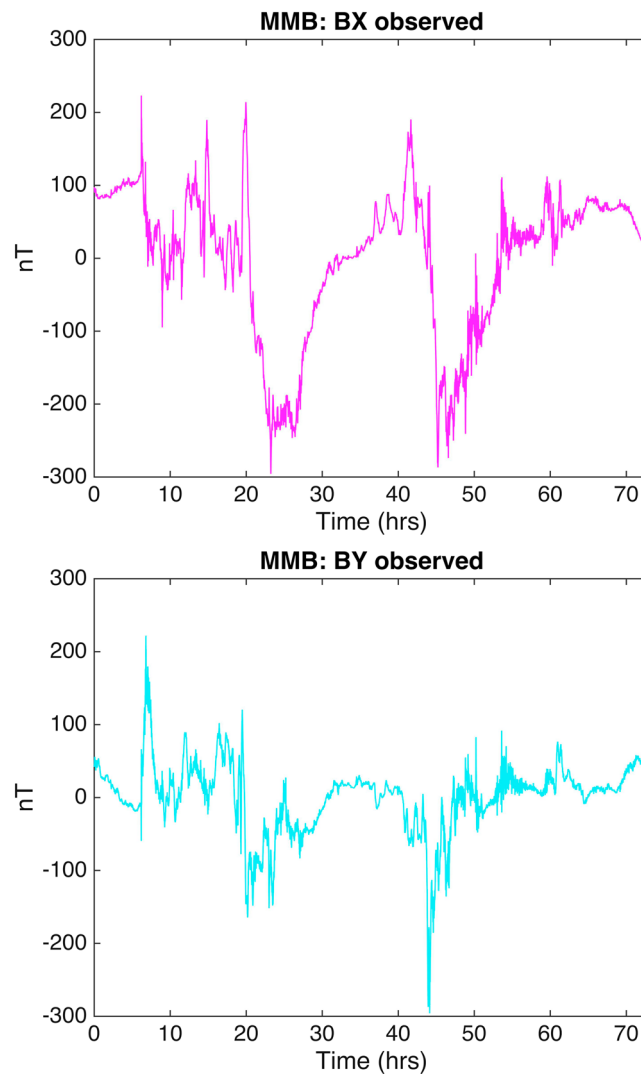
Figure 4. Plotted is the 1 s geomagnetic field time series for 3 days from the onset of the Halloween storm, as measured by the Memambetsu magnetic field observatory in Japan, B_x (south to north) and B_y (west to east). Best fitting linear trend had been removed from the time series before further processing was applied.

except that now the full 3 days of the data are plotted. The DTIR estimated geoelectric field (shown in green) does not start until after the first 6 h of the time series, reflecting the length of the impulse response filter and the convolution process. In Figure 6 (bottom left) and 6 (bottom right), we plot the deviations in the estimate relative to the observations, on a different scale that would best allow a visual analysis. We can immediately see that the estimation errors never exceed 15% of the signal, and the error magnitudes are similar between the two methods. We further refer the reader to Figure 7 to note that by band-pass filtering all geoelectric field time series to the period range from 10 s to 12 h (twice the length of DTIR window, and likely the extent of validity of MT impedance), we further reduce the magnitudes of our misfits to generally no more than 5% of the (filtered) signal.

To better quantify the errors, let us define the correlation coefficient between two discrete time series $p = (p_1, p_2, \ldots, p_N)$ and $t = (t_1, t_2, \ldots, t_N)$, with $\bar{p} = \frac{1}{N} \sum_{i=1}^{N} p_i$ and $\bar{t} = \frac{1}{N} \sum_{i=1}^{N} t_i$, as

$$CC = \frac{\Sigma_1^N (p_i - \bar{p})(t_i - \bar{t})}{\sqrt{\left(\sum_{i=1}^{N} (p_i - \bar{p})^2\right)} \sqrt{\left(\sum_{i=1}^{N} (t_i - \bar{t})^2\right)}}.$$
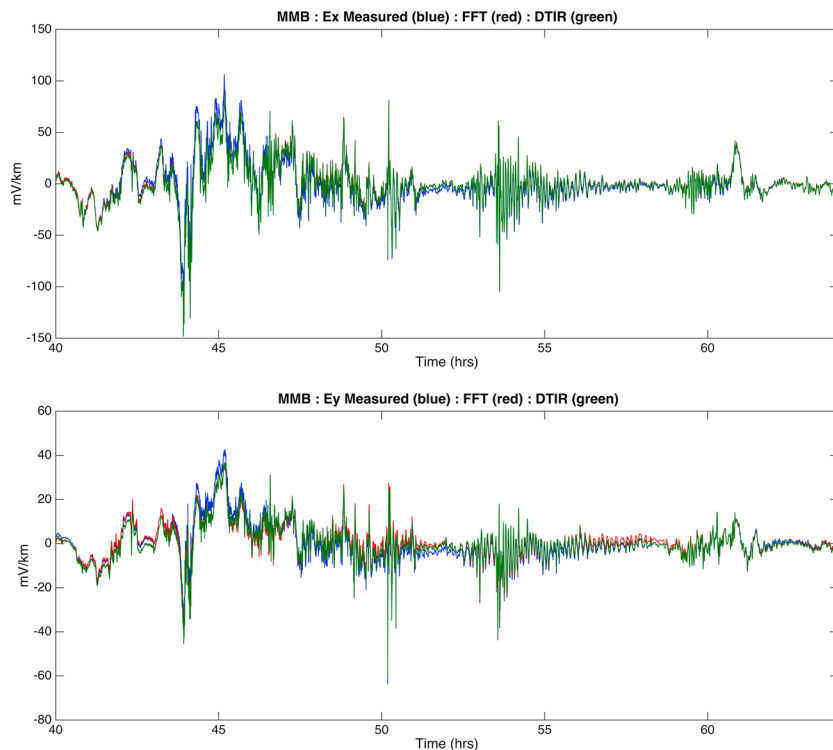
Figure 5. Close-up of the most intense 24 h of the Halloween storm as measured by the Memambetsu magnetic field observatory in Japan. Time is recorded in hours from 29 October 2003 at 00:00:00 UTC. Plotted are measured 1 s geoelectric field time series (in blue) versus the estimated geoelectric field using DTIR (green), as well as using a Fourier transform approach in frequency domain (red). All estimates employed the full 3-D MT response. All time series have been detrended. No additional filtering has been applied to these time series. (top) E_x (south to north). (bottom) E_y (west to east).

Additionally, if p denotes the prediction and t denotes the target time series, we follow *Weigel* [2017] in defining the prediction efficiency (PE) as PE = 1 − ARV, where the average relative variance

$$\text{ARV} = \frac{\frac{1}{N}\sum_{i=1}^{N}(p_i - t_i)^2}{\sigma_t^2}, \tag{15}$$

where σ_t^2 is the variance of the target time series t. Perfect correlation and perfect fit would correspond to the values of 1 for both. The goodness of correlation and fit is quantified in Table 1.

6. Discussion

Multiple factors contribute to discrepancies that might occur between estimated and measured geoelectric field data. Naturally occurring processes in the ground include electrochemical interactions between minerals and subsurface fluids, as well as the flow of ionic fluids, and thermoelectric mechanisms caused by temperature gradients in the subsurface. Such transient signals in measured geoelectric data can last minutes to hours, and due to their noninductive nature we cannot expect to reproduce them with a geoelectric field estimation algorithm. Other effects of non-plane wave inductive nature are not typically reflected in the estimated MT response. Variations of loads in power lines and electric trains, for example, are sources of cultural noise in measured geoelectric field data. Diurnal signals in geoelectric field measurements are further caused by local temperature variations, while other longer-term effects are caused by factors such as charge buildup in the electrodes and the thermal electric potential. Coastal geoelectric field measurements are also affected by motional induction due to ocean tides. Most of these effects would not be observed in the measured geomagnetic field time series that we use to obtain our estimates, nor do they matter from a GIC perspective, but they do contribute to the misfits observed during a validation exercise that involves real geoelectric field data.
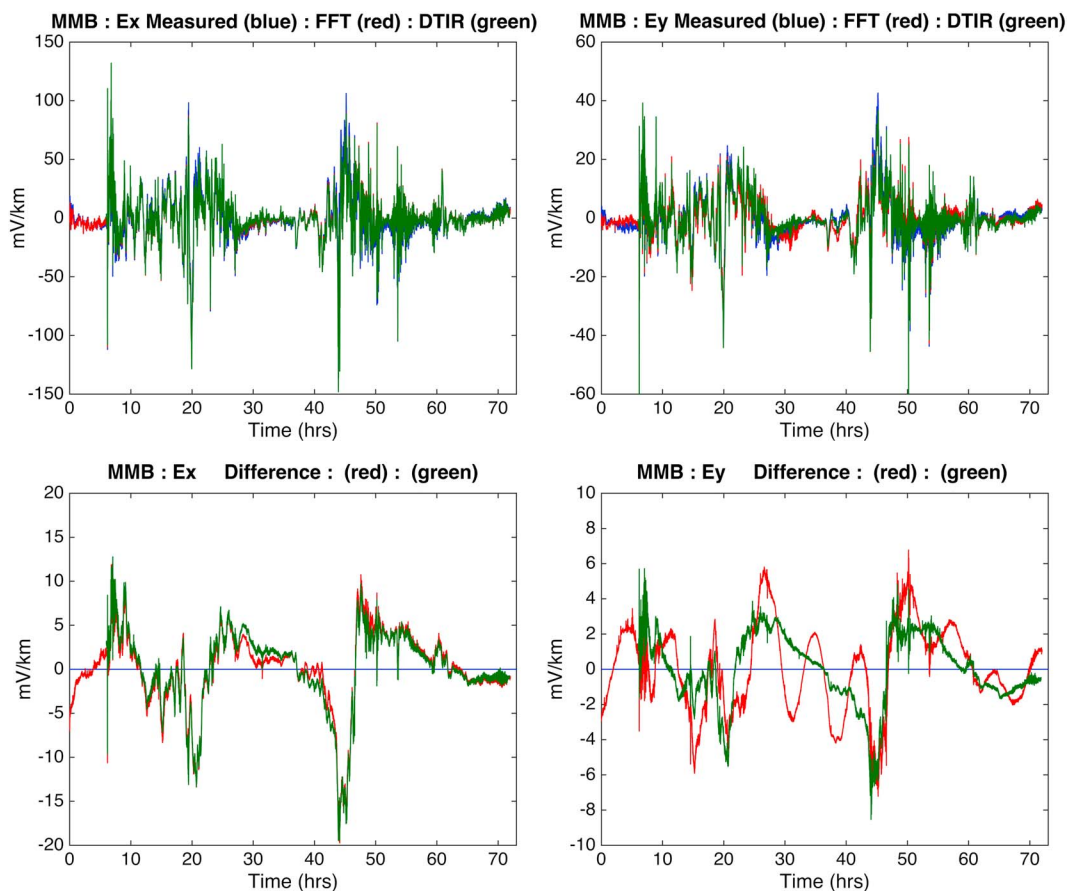
Figure 6. Plotted are 1 s geoelectric time series for 3 days from the onset of the Halloween storm at the Memambetsu magnetic field observatory in Japan. (top left) E_x measured (blue) versus estimated using DTIR (green) and estimated using a Fourier transform approach in frequency domain (red), all using the full 3-D MT response. (bottom left) The absolute difference in E_x (estimated minus measured), on a different scale. (top right and bottom right) Same as Figures 6 (top right) and 6 (bottom right) but for E_y. No filtering has been applied to these time series.

There are additional constraints that are associated with using an MT response tensor as the "filter" to obtain the geoelectric field. Both geomagnetic and geoelectric time series are discrete and finite and therefore require filtering before the MT response is constructed. The MT response is therefore band limited, and accurate estimation of geoelectric fields outside of the constraints of the empirical MT response is not, in general, feasible. Moreover, at the lower and upper stretches of the MT response period range, the measured geoelectric time series are affected by the measurement system filtering configuration. At short periods, the discrete sampling of geoelectric field measurements requires the use of filtering. This is typically dealt with in MT instruments by employing built-in low-pass filters. For example, the 1 s time series of the geoelectric and geomagnetic fields at Memambetsu are influenced by measurement systems at periods shorter than several

Table 1. Goodness of Fit for Estimated Geoelectric Time Series Versus Geoelectric Field Measured by the Electrodes in the Ground, as Quantified by the Correlation Coefficient (CC) and the Prediction Efficiency (PE) Measures[a]

	1-D FFT: CC	3-D FFT: CC	3-D DTIR: CC	1-D FFT: PE	3-D FFT: PE	3-D DTIR: PE
E_x (no filters)	0.6722	0.9742	0.9731	0.9998	1.0000	1.0000
E_y (no filters)	0.8182	0.9458	0.9657	0.9908	0.9997	0.9998
E_x (band pass)	0.8764	0.9867	0.9928	0.9999	1.0000	1.0000
E_y (band pass)	0.8244	0.9561	0.9856	0.9889	1.0000	1.0000

For 1-D comparison, best fitting 1-D regional model from [*Pulkkinen et al.*, 2010] was employed (see Appendix A for details of the data fits)
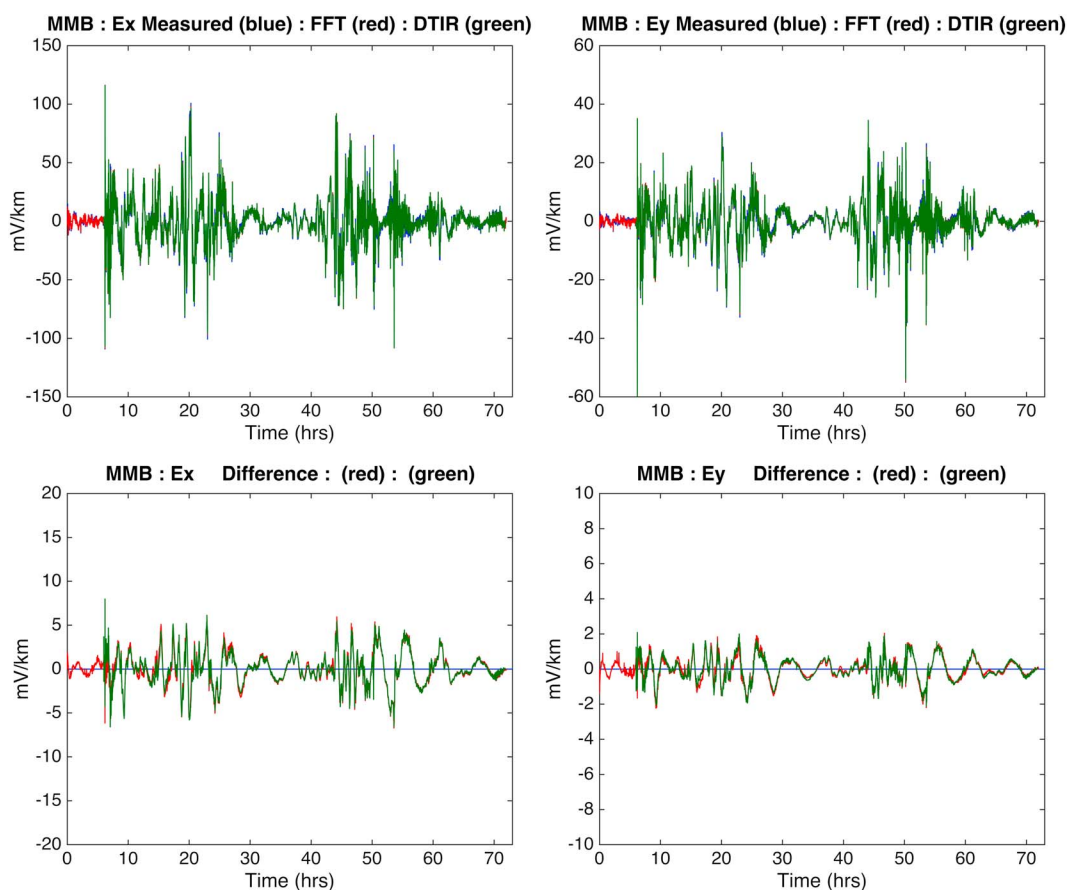
Figure 7. Plotted are 1 s geoelectric time series for 3 days from the onset of the Halloween storm at the Memambetsu magnetic field observatory in Japan. (top left) E_x measured (blue) versus estimated using DTIR (green) and estimated using a Fourier transform approach in frequency domain (red), all using the full 3-D MT response. (bottom left) The absolute difference in E_x (estimated minus measured), on a different scale. (top right and bottom right) Same as Figures 7 (top right) and 7 (bottom right) but for E_y. All time series have been band-pass filtered for this plot, with the sharp cutoffs at 10 s and 12 h.

tens of seconds. On the other hand, the MT responses at Memambetsu at periods shorter than 30 s have already been corrected for system filter configuration. So this could result in very high frequency discrepancies between the observed and predicted 1 s geoelectric data.

By contrast, the longest periods, which are transmitted farthest, are also most likely to be affected by various large-scale processes such as a buildup of charge at interfaces (e.g., coastlines) with large conductivity contrasts, long-term temperature variations and water movement in the ground, just as the geoelectric field signal is getting weaker. A high-pass filter is often used to filter out diurnal signals that are primarily thermal. Longer-period geoelectric fields are also most affected by non-plane wave ionospheric sources such as Sq variations. The MT response uses a uniform source approximation and should not in general be able to account for Sq variations.

In spite of an overall excellent fit and correlation shown in section 5, we do however notice coherent structure in the misfits in Figure 6 that we are not able to reproduce with either of the two independently developed methods. This additional signal constitutes as much as 10–15% of the magnetic storm signal at its peak. We believe that such artifacts are an inherent limitation of our approach: specifically, certain physical processes contributing to measured, surface geoelectric fields cannot be recovered from the local geomagnetic field measurement obtained at a single point, in conjunction with an MT response. Alternative approaches might be developed that would account for the regional inhomogeneity of storm time ionospheric sources, and their inductive effects. Such effects would cause very large scale currents in the Earth's lithosphere, especially in the presence of conductivity contrasts. It is therefore not surprising that our misfits are dominated by longer
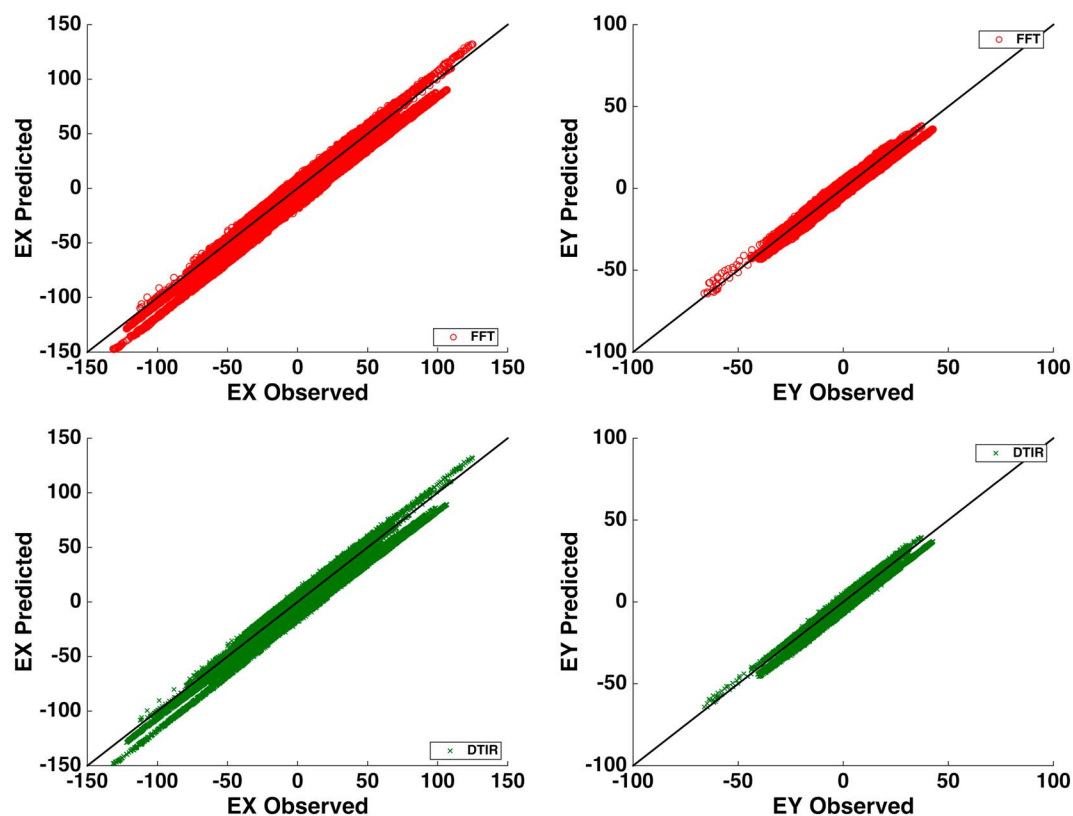
Figure 8. Scatterplots for the 1 s geoelectric time series for 3 days from the onset of the Halloween storm at the Memambetsu magnetic field observatory in Japan. (top left) E_x estimated using FFT approach. (top right) E_y estimated using FFT approach. (bottom left) E_x estimated using DTIR approach. (bottom right) E_y estimated using DTIR approach.

periods. In fact, if we band-pass filter both the measured and estimated geoelectric time series to the period range of 10 s to 12 h, which most certainly limits the validity of the MT impedance under the usual plane wave assumptions, the misfits are reduced to no more than 5% of the signal (Figure 7). The coherence and nonstationarity of our misfits, as well as an overall excellent data fit, can also be vividly observed in the scatter plots of Figure 8.

In applying this technique to more traditional MT responses such as the EarthScope MT data set [*Schultz et al.*, 2006-2018], one needs to be even more careful in comparison with measured data, as additional complexities come into play in trying to measure (and reproduce) ground geoelectric field data in an array-style temporary installation. Collection of noise-free geoelectric field data becomes very difficult in proximity to most human activity or a power line. In such areas, data spikes and cultural noise sometimes overwhelm geoelectric field measurements to an extent that the estimation of the geoelectric field using a real-time geomagnetic field measurement and a clean MT response may give more accurate results than direct geoelectric field as measured. Electric fields in USArray data set are also highly susceptible to temperature-related variations, which further contaminates (and eventually, dominates) the long-period structure (at a permanent observatory installation such as Memambetsu, the electrodes are buried deeper and are not affected by temperature as much as the electrodes at the MT sites are). With certain specific site exceptions, reproduction of the long-period signal in the measured geoelectric field is ill-advised because it is predominantly a temperature-driven effect and would not (in reality) affect GICs, which typically have the most power in the period range of 1 to 1000 s.

7. A Note on Causality and Real-Time Electrical Field Estimation

As is shown by *Egbert* [1992], even in a simple 1-D situation for which its continuous counterpart has been shown to be causal, DTIR exhibits numerical noncausality. In practice this means that the modeled geoelectric field $\mathbf{E}_t$ at time t_0 depends not only on the present and past states of the geomagnetic field $\mathbf{B}_t$, but also on a few
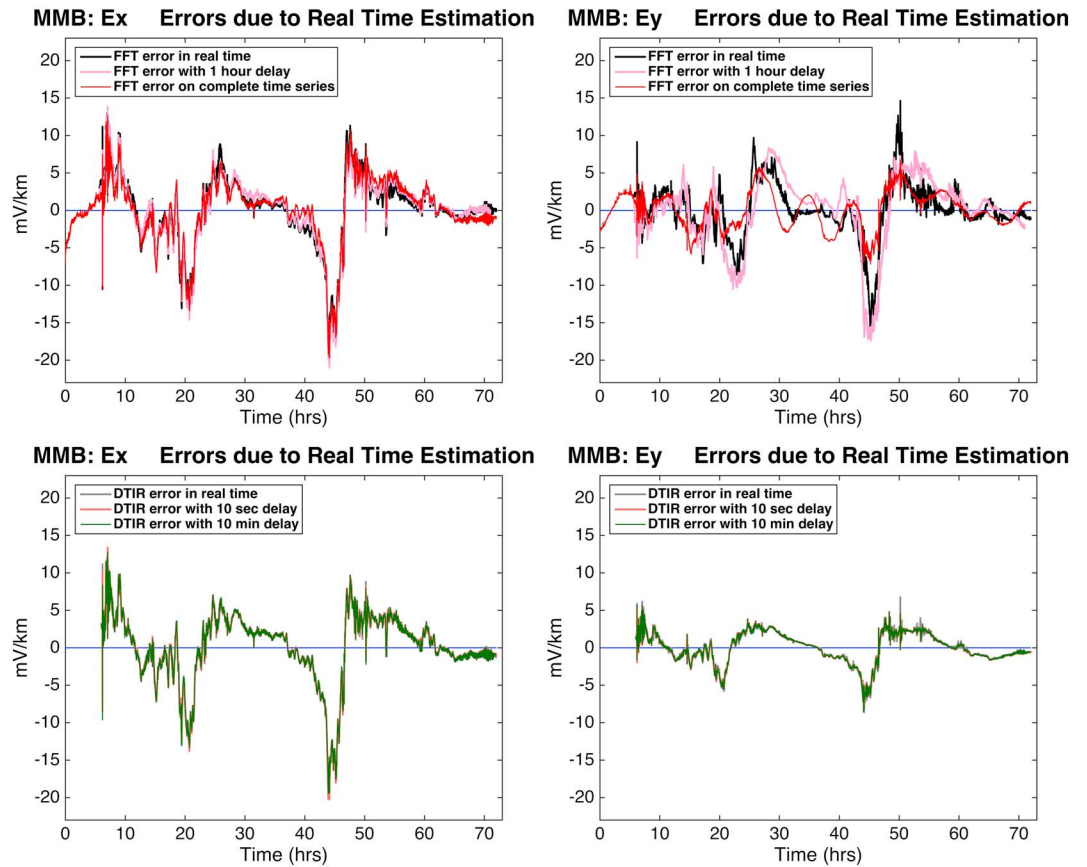
Figure 9. Prediction errors for the Halloween storm in the (left column) E_x (south to north) and (right column) E_y (west to east) geoelectric field components due to running the FFT and DTIR algorithms, respectively, in real time. The real-time errors are compared with the errors shown in Figure 6. In this case, a sliding window real-time FFT does not degrade accuracy in E_x but amplifies E_y errors by a factor of 2. Running DTIR in real time introduces high-frequency noise in the prediction that is hardly noticeable in this figure (see Figure 11).

of its future states. In a general 3-D situation, both the geomagnetic and geoelectric field are causally affected by the ionospheric source current, however strict causality of the relationship between the total geomagnetic and total geoelectric fields has been debated in the literature [e.g., *Egbert*, 1990; *Berdichevsky*, 1999; *Alekseev et al.*, 2009] and has never been shown to hold in general. The analysis in section 5 has been performed with what would equate to a 10 min delay in a real-time geoelectric field estimation service, to take this effect into account. This can potentially create a problem for a data service that aims to provide the geoelectric
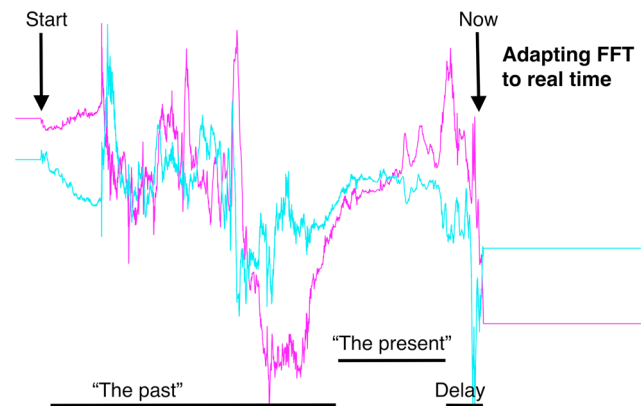

Figure 10. A schematic to illustrate the algorithm to adapt the FFT method to real time.
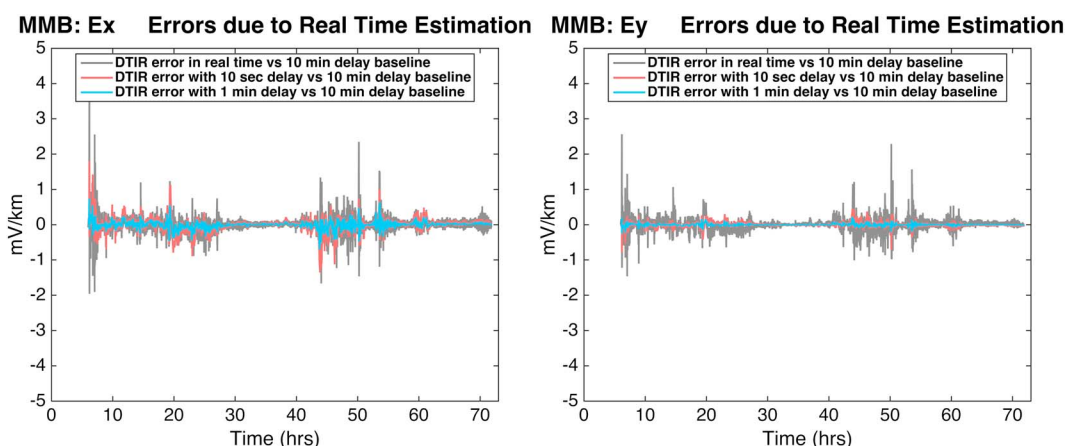
Figure 11. High-frequency noise in DTIR geoelectric field predictions for the Halloween storm in the (left) E_x (south to north) and (right) E_y (west to east) due to forcing strict causality in DTIR (zero negative lag, in gray) or truncating the negative lag to a shorter time window of 10 s (in peach) and 1 min (in light blue), respectively. As is evident from this plot, a modest prediction delay of 1 min or less eliminates most of the high-frequency noise.

field estimates as soon as the measured geomagnetic field is available. Noncausality of the algorithm will by necessity introduce an additional prediction delay into such an algorithm. From this point of view, it is useful to briefly explore the extent of noncausality that is involved. The results of this analysis are presented in this section. We first of all convert the algorithms of sections 3 and 4 to real time.

The FFT algorithm (section 3) is typically applied to a known segment of the time series. This is equivalent to constructing a periodic time series where the given segment is infinitely repeated. In section 3, we dealt with the edge effects at the ends of the segment by "padding" both ends with their end value for a certain length of time. This is, then, equivalent to assuming that the time series stays constant from the given time, "now," for a stretch of time. In a real-time application of this method to 1 s data, we take 10 point steps and use a sliding time window of 20,480 s. At each step, we assume that the last value that is known repeats itself into the future. We then perform the FFT geoelectric field estimation on this time segment and compare the last 10 points only with those that we would have obtained, had we known the future at the time of computation, as we assumed in section 5. Figure 9 illustrates the estimation errors of this real-time algorithm, as compared to the errors discussed in section 5. For a 1 h delay variant of this FFT real-time estimation that is also shown in Figure 9, we assume that we know the future 1 hour of data, and only then do we pad. This procedure is illustrated in Figure 10. In this case, application of FFT in real time does not affect the accuracy of E_x estimates, but multiplies the errors in E_y by a factor of 2, resulting in a 25% maximum error during the more intense phases of the storm.

The DTIR approach (section 4) is natively suited for real-time application. For this analysis, we merely constrain the DTIR to have a shorter negative lag than in section 4 (which was 10 mins or 600 samples), and proceed to solve the linear system (12) under these constraints. Here we consider two variants of DTIR, computed with no negative lag (i.e., real time), and a 10 s negative lag (resulting in a corresponding prediction delay). In Figure 9, we compare these two variants of DTIR geoelectric field estimation with that employed in section 5. Estimation errors are not noticeably affected by a real-time application of the method. Nevertheless, low-amplitude, high-frequency noise is introduced in the estimates when we apply DTIR algorithm in real time. We zoom in on this effect in Figure 11.

As is evident from Figure 11, forcing strict causality upon a DTIR is essentially equivalent to introducing high-frequency noise in the geoelectric field estimate. The amplitude of the noise is of the order of a few percent of the total E field amplitude but will vary depending on the structure of the MT response, the sampling of the time series, and the type of regularization used to obtain DTIR. Our analysis shows that, in general, the use of the log linear smoothing in the DTIR estimation allows us to mitigate much of the unfortunate effects of the causal DTIR truncation on the shorter periods in the E field time series prediction (see Appendix B). We can also eliminate the bulk of the noise by allowing for a modest 10 s time lag in geoelectric field prediction. A 1 minute time lag provides no more than a little additional benefit in terms of accuracy.

8. Conclusions

Extreme magnetic storms can be hazardous for ground-based infrastructure, potentially resulting in a significant economic disruption in the United States, as well as globally. The hazards associated with space weather call for a national service that would provide real-time estimates as well as predictions of the relevant ground level geoelectric fields. Ground-level geoelectric fields, if estimated with sufficient accuracy and in a timely manner, would help the power grid industry and other affected entities to take prompt action that would mitigate infrastructure damage.

This manuscript focuses on the development of a discrete time domain impulse response (DTIR) methodology for geoelectric field estimation using a geomagnetic field data stream, and a fully 3-D MT response of the Earth. We apply this methodology to the Halloween storm measurements in Japan and validate our geoelectric field estimates using both the frequency domain approach and the measured data. We demonstrate in section 5 that both the newly developed time domain and the frequency domain methods are equally accurate for storm time geoelectric field estimation, with errors to within 10–15% of peak geoelectric field amplitude for our sample storm and geographic location.

An important word of warning is of note. We have seen that while we are able to recover as much as 85–90% of the geoelectric field signal throughout our case study, additional long-period structure is present in the geoelectric fields during storm times that cannot be recovered (sections 5 and 6). We suggest that there can be inherent limitations to using traditional MT responses to compute storm time geoelectric fields but that these are not prohibitive for operational geoelectric field estimation, as long as the full 3-D MT response is employed.

We have also briefly considered the issue of causality in a time domain geoelectric field prediction algorithm. We show that for the MT response we consider in this paper, a delay of as little as 10 s might be sufficient with very little loss in prediction accuracy. Enforcing strict causality, however, introduces a certain amount of high-frequency noise in the predicted geoelectric field (a few percent of the signal, section 7). By contrast, applying the frequency domain algorithm in close to real time leads to additional estimation errors of up to 10% of the signal (Figure 9). We conclude that while both approaches can be successfully applied in real time, a time domain approach such as the one developed in this manuscript, applied with a modest estimation delay results in the smallest errors in real-time geoelectric fields.

In addition to using MT response functions estimated from empirical data, they can also be obtained from a model of regional electrical conductivity structure. Employing a regional 1-D conductivity profile has not been shown to produce an accurate estimate of the local geoelectric field [e.g., *Weigel*, 2017] due to the highly variable Earth conductivity within regions [e.g., *Bedrosian and Love*, 2015]. It is nevertheless conceivable that 1-D inversion of GIC itself [see, e.g., *Pulkkinen et al.*, 2007] and the predicted 1-D response obtained from it at certain locations might provide a better regional representation of geoelectric field, more directly relevant to observed GICs, than any single local empirical MT response. This possibility arises from the fact that empirical MT responses are often significantly affected by very small scale, anomalously high or low conductivity features in the immediate vicinity of the site, a phenomenon known as distortion. Because GICs flow along grounded power lines over a significantly larger area, the quantity of interest is the integrated electric field along that path. Therefore, certain averaging is involved in going from local electric field estimates to GIC computations. We should therefore caution against using a local empirical MT response to estimate a regional geoelectric field. Instead, local geoelectric field values should be obtained at a number of points along the path of the grounded power line, ideally using a high-resolution 3-D electrical conductivity model and averaged to obtain the GIC correlate.

This analysis can be readily applied in the United States. While using the USArray MT responses [*Schultz et al.*, 2006-2018] for geoelectric field computations would constitute a great improvement over the current practice [see, e.g., *Bedrosian and Love*, 2015; *Weigel*, 2017; *Bonner and Schultz*, 2017], a much better solution is to obtain the synthetic, modeled responses on a fine regular grid and use these for real-time geoelectric field computations. This strategy potentially provides a means to eliminate the distortion from the MT response estimates, allowing for better predictive power. We outline this approach as a useful future direction for research. In fact, it is the intention of the USGS Geomagnetism Program to obtain such synthetic MT responses and to keep releasing annual updates to the community, as better electrical conductivity models become available. Having said that, any model of ground conductivity is only as good as the data that come into it. There is no substitute for completing the USArray MT survey.

9. Data Resources

Measured magnetic and electric time series are freely available from the International Real-Time Magnetic Observatory Network (INTERMAGNET; http://www.intermagnet.org/data-donnee/download-eng.php). The processed MT responses [*Fujii et al.*, 2000-2011] will be made available at SPUD EMTF (http://ds.iris.edu/spud/emtf) in conjunction with the publication of this manuscript.

Appendix A: Electric Fields Using Best Fitting Regional 1-D Model

The location of Memanbetsu geomagnetic observatory makes it an exemplary site to illustrate the effects of three-dimensionality of the Earth conductivity on the local geoelectric fields. An earlier study by *Pulkkinen et al.* [2010] obtained the best regional 1-D model of Earth's electrical conductivity at the site. This model, in conjunction with certain power grid system-specific parameters, does a good job of reconstructing the measured GIC in the system. However, as we can see in Figure A1, the best fitting regional 1-D model provides us with an MT response that does not reconstruct the measured local electric fields at the site with precision comparable to what the 3-D MT response provides (Figure 6). While still correlated with the signal (Table 1), the amplitudes of the misfits are of about the same magnitude as those of the measured signal. This suggests to us that while a regional 1-D model may still be useful for regional GIC modeling, it is of limited utility for local geoelectric field estimation. Conversely, a single-point geoelectric field estimate or measurement, in general, contains insufficient information for regional GIC computations. Instead, geoelectric field estimates at multiple locations are required. The 3-D effects observed in these estimates may be smoothed out to some
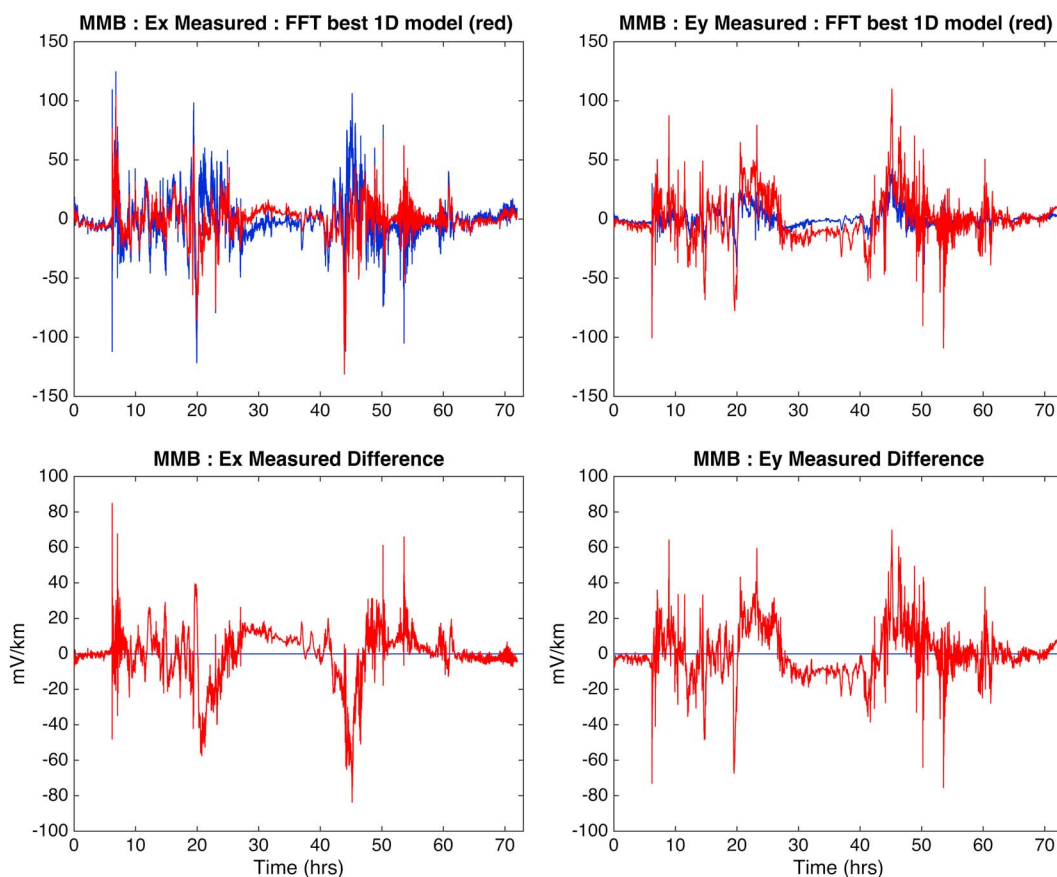

Figure A1. Plotted are 1 s geoelectric time series for 3 days from the onset of the Halloween storm at the Memambetsu magnetic field observatory in Japan. (top left) E_x measured (blue) versus estimated a Fourier transform approach in frequency domain (red) using a best fitting 1-D conductivity profile of *Pulkkinen et al.* [2010]. (bottom left) The absolute difference in E_x (estimated minus measured), on a different scale.(top right and bottom right) Same as Figures A1 (top left) and A1 (bottom left) but for E_y. Note that even though the measured and predicted signals are correlated (Table 1), the magnitudes of the misfits are comparable to those of the measured data.

extent when the fields are integrated along a power line for GIC computations, but that would depend on the location and orientation of the power line relative to the geometry of Earth structures. Earlier 1-D-based GIC studies could be revisited with the updated information to explore this issue.

Appendix B: Regularization of DTIR

As we discussed in section 4, discrete time impulse response $\mathbf{z}_t$ can be obtained by solving the linear system (14). This is a system of N_t equations, with N_t unknowns (the real-valued entries of vector $\mathbf{z}_t$). The matrix A is $8N_f \times N_t$ and defines, essentially, discrete Fourier transform as in equation (11) (with entries $\exp(-i2\pi f_m t_k)$ corresponding to the mth frequency and the kth impulse response sample). The matrix Σ is $8N_f \times 8N_f$ and defines the covariance of the MT response components. In our implementation, Σ is diagonal and populated with variances of the four MT response components, real and imaginary parts, for each frequency. The full MT response covariance could also be used. The matrix Q, which determines the regularization, is $N_t \times N_t$. We tested two variants proposed by *Egbert* [1992]:

$$Q_{kl} = \delta_{kl} k^4, \tag{B1}$$

which achieves regularization of DTIR that corresponds to linear smoothing in the frequency domain, and

$$Q_{kl} = \begin{cases} 1 & \text{if } k = l = 0 \\ k^2\pi^2/2 + k^4\pi^4/4 & \text{if } k = l \neq 0 \\ (2 - 3\pi^2 kl)\alpha + 12\alpha^2 - \pi^2 kl & \text{if } k - l \text{ is odd} \\ kl\pi^2(1 + 3\alpha) & \text{if } k - l \text{ is even} \end{cases}, \tag{B2}$$

where $\alpha = kl/((k-l)^2)$, which achieves a DTIR that corresponds to a spline fit in log frequency (i.e., log linear smoothing). We further multiply this variant of Q by the factor 1e+9 to give the damping parameter λ similar meanings for both variants of Q.

We found the choice of Q to be key in the accurate computation of DTIR, especially as it pertains to the fit at extremely long periods that greatly exceed 10,000 s. At such long periods, linear smoothing (B1) is no longer an appropriate regularization for the DTIR least squares fit. A relaxed linear smoothing allows us to fit the long periods, but introduces artificial signal in the midperiod band. On the other hand, a stronger linear smoothing first decreases the fit at the longest periods and only then addresses the midperiod artifacts. Using the log linear regularization (B2) gives significantly better results, fitting the longest periods adequately with a smooth frequency domain curve as in Figures 2 and 3, provided that the length of the impulse response window $[N_{t-}, N_{t+}]$ is sufficient to capture the bulk of the signal. As discussed in section 5, for a 1 s time series sampling, a 6 h window ($N_{t+} = 21,600$) was empirically found to be sufficient to produce a good fit for periods up to 200,000 s.

Appendix C: Optimizing the Implementation of DTIR

As is discussed in Appendix B, fitting the MT response at longer periods (beyond 10,000 s) requires a rather long time series ($N_t > 20,000$) to represent the DTIR adequately for 1 s data sampling. Numerical solution of the linear system (14), also known as the *model space formulation*, which has N_t unknowns, becomes computationally expensive, as well as ill-conditioned. For example, a linear inversion for a DTIR of length $\approx$10,000 s requires approximately 5 min run time in Matlab on a modern laptop or desktop; anything much bigger than that challenges the computer memory limits. (By contrast, we find that DTIR time window from negative 10 min to positive 2 h (or [−600 7200]) is sufficient to fit all USArray MT responses, which span the period range from 7 s to 20,000 s.)

The alternative *data space formulation*,

$$(AQ^{-1}A^T + \lambda\Sigma^{-1})\mathbf{b}_\lambda = \mathbf{z}_f, \tag{C1}$$

with $\mathbf{z}_t = Q^{-1}A^T\mathbf{b}_\lambda$ is equivalent and has none of these limitations. This formulation has $8N_f$ unknowns (typically $\gg N_t$) and requires 3 s run time in Matlab for an equivalent problem. In fact, this alternative approach is so efficient that optimality can easily be achieved by solving the linear system (C1) repeatedly for a range

of values of the damping parameter λ and then choosing a solution based on an L curve or a discrepancy principle (i.e., opting for the smoothest solution that still fits the data to within the chosen misfit threshold).

We note, however, that this alternative formulation requires an inverse of the Q matrix discussed in Appendix B. This inverse is trivial for the diagonal Q of equation (B1) but is less than trivial for the full matrix of equation (B2), which we have chosen to use for this manuscript. This precludes us from using the more efficient data space formulation with an L curve for the Japanese observatory DTIR obtained in section 5. Instead, we empirically found a value of damping parameter λ that allows us to fit the MT response well and not introduce any midperiod artifacts, using the log linear smoothing in model space as described by equations (14) and (B2). A relatively straightforward extension of the technique to compute Q^{-1} for (B2) would allow for a data space formulation with a log linear smoothing that would increase computational efficiency. We note that Q^{-1} needs only to be computed once and may then be reused.

References

Albertson, V. D., et al. (1993), Geomagnetic disturbance effects on power systems, *IEEE Trans. Power Delivery*, *8*, 1206–1216.

Alekseev, D., N. Palshin, and I. M. Varentsov (2009), Magnetotelluric dispersion relations in a two-dimensional model of the coastal effect, *Izv. Phys. Solid Earth*, *45*(2), 167–170.

Allen, J., L. Frank, H. Sauer, and P. Reiff (1989), Effects of the March 1989 solar activity, *Eos Trans. AGU*, *70*(46), 1479–1488.

Baker, D. N., et al. (2008), *Severe Space Weather Events — Understanding Societal and Economic Impacts*, 1–144 pp., Natl. Acad. Press, Washington, D. C.

Bedrosian, P. A., and D. W. Feucht (2014), Structure and tectonics of the Northwestern United States from EarthScope USArray magnetotelluric data, *Earth Planet. Sci. Lett.*, *402*, 275–289, doi:10.1016/j.epsl.2013.07.035.

Bedrosian, P. A., and J. J. Love (2015), Mapping geoelectric fields during magnetic storms: Synthetic analysis of empirical United States impedances, *Geophys. Res. Lett.*, *42*(23), 10,160–10,170, doi:10.1002/2015GL066636.

Béland, J., and K. Small (2005), Space weather effects on power transmission systems: The Cases of Hydro-Québec and Transpower New ZealandLtd, in *Effects of Space Weather on Technology Infrastructure*, edited by I. A. Daglis, pp. 287–299, Springer, Dordrecht, Netherlands.

Berdichevsky, M. (1999), Marginal notes on magnetotellurics, *Surv. Geophys.*, *20*(3–4), 341–375.

Bolduc, L. (2002), GIC observations and studies in the Hydro-Québec power system, *J. Atmos. Sol. Terr. Phys.*, *64*, 1793–1802.

Bonner, L. R., and A. Schultz (2017), Rapid prediction of electric fields associated with geomagnetically induced currents in the presence of three-dimensional ground structure: Projection of remote magnetic observatory data through magnetotelluric impedance tensors, *Space Weather*, *15*, 204–227, doi:10.1002/2016SW001535.

Boteler, D. (2012), On choosing Fourier transforms for practical geoscience applications, *Int. J. Geosci.*, *3*, 952–959.

Boteler, D. H. (2001), Assessment of geomagnetic hazard to power systems in Canada, *Nat. Hazards*, *23*, 101–120.

Boteler, D. H. (2003), Geomagnetic hazards to conducting networks, *Nat. Hazards*, *28*, 537–561.

Bracewell, R. N. (2000), *The Fourier Transform and its Applications*, pp. 1–616, McGraw-Hill, New York.

Cagniard, L. (1953), Basic theory of the magneto-telluric method of geophysical prospecting, *Geophysics*, *18*(3), 605–635.

Chave, A. D. (2012), Estimation of the magnetotelluric response function, in *The Magnetotelluric Method*, edited by A. D. Chave and A. G. Jones, pp. 165–218, Cambridge Univ. Press, Cambridge, U. K.

Chave, A. D. (2014), Magnetotelluric data, stable distributions and impropriety: An existential combination, *Geophys. J. Int.*, *198*, 622–636, doi:10.1093/gji/ggu121.

Chave, A. D., and A. G. Jones (2012), *The Magnetotelluric Method: Theory and Practice*, Cambridge Univ. Press, New York.

Chave, A. D., D. J. Thomson, and M. E. Ander (1987), On the robust estimation of power spectra, coherences, and transfer functions, *J. Geophys. Res.*, *92*(B1), 633–648.

Egbert, G. D. (1990), Comments On 'Concerning dispersion relations for the magnetotelluric impedance tensor' By E. Yee and K. V. Paulson, *Geophys. J. Int.*, *102*, 1–8.

Egbert, G. D. (1992), Noncausality of the discrete-time magnetotelluric impulse response, *Geophysics*, *57*, 1354–1358.

Egbert, G. D., and J. R. Booker (1986), Robust estimation of geomagnetic transfer functions, *Geophys. J. R. Astron. Soc.*, *87*(1), 173–194.

Egbert, G. D., and A. Kelbert (2012), Computational recipes for electromagnetic inverse problems, *Geophys. J. Int.*, *189*, 251–267, doi:10.1111/j.1365-246X.2011.05347.x.

Federal Energy Regulatory Commission (FERC) (2013), Reliability standards for geomagnetic disturbances, Fed. Energy Reg. Comm., *Federal Register, Rules and Regulations*, *79 FR*(35911), 35,911–35,920.

Federal Energy Regulatory Commission (FERC) (2016), Reliability standard for transmission system planned performance for geomagnetic disturbance events, Fed. Energy Reg. Comm., *Federal Register, Rules and Regulations*, *81 FR*(67120), 67,120–67,140.

Ferguson, I. J., and H. D. Odwar (1997), Review of conductivity soundings in Canada, Appendix 3, in *Geomagnetically Induced Currents: Geomagnetic Hazard Assessment, Phase II, 357 T 848A*, vol. 3, edited by D. H. Boteler, pp. 1–121, Geol. Surv. Canada and Canadian Electr. Assoc.

Fernberg, P. (2012), *One-Dimensional Earth Resistivity Models for Selected Areas of Continental United States and Alaska*, pp. 1–190, EPRI Technical Update 1026430, Palo Alto, Calif.

Fujii, I., T. Ookawa, S. Nagamachi, and T. Owada (2000-2011), Long-period magnetotelluric transfer functions from geomagnetic observatories at Kakioka, Kanoya and Memambetsu, Japan, doi:10.17611/DP/EMTF/INTERMAGNET/JMA.

Fujii, I., T. Ookawa, S. Nagamachi, and T. Owada (2015), The characteristics of geoelectric fields at Kakioka, Kanoya, and Memambetsu inferred from voltage measurements during 2000 to 2011, *Earth Planets Space*, *67*, 62, doi:10.1186/s40623-015-0241-z.

Gannon, J. L., L. Trichtchenko, and P. Fernberg (2012), United States regional GIC hazard assessment, Abstract SM21D-08 presented at 2012 Fall Meeting, AGU, San Francisco, Calif.

Gannon, J. L., C. C. Balch, and L. Trichtchenko (2013), Regional United States electric field and GIC hazard impacts, Abstract SM52C-04 presented at 2013 Fall Meeting, AGU, San Francisco, Calif.

Groom, R. W., and R. C. Bailey (1989), Decomposition of magnetotelluric impedance tensors in the presence of local three-dimensional galvanic distortion, *J. Geophys. Res.*, *94*(B2), 1913–1925.

Kappenman, J. G., W. A. Radasky, J. L. Gilbert, and L. Erinmez (2000), Advanced geomagnetic storm forecasting: A risk management tool for electric power system operations, *IEEE Trans. Plasma Sci.*, *28*(6), 2114–2121.

Kelbert, A., G. D. Egbert, and A. Schultz (2011), IRIS DMC data services products: EMTF, the magnetotelluric transfer functions. [Available at http://ds.iris.edu/spud/emtf/.]

Lam, H.-l. (2011), From early exploration to space weather forecasts: Canada's geomagnetic odyssey, *Space Weather*, *9*, 1–5, doi:10.1029/2011SW000664.

Love, J. J., and A. Chulliat (2013), An international network of magnetic observatories, *Eos Trans. AGU*, *94*(42), 373–384, doi:10.1002/2013EO420001.

Love, J. J., and C. A. Finn (2011), The USGS Geomagnetism Program and its role in space weather monitoring, *Space Weather*, *9*, S07001, doi:10.1029/2011SW000684.

Love, J. J., E. J. Rigler, A. Pulkkinen, and C. C. Balch (2014), Magnetic storms and induction hazards, *Eos Trans. AGU*, *95*(48), 445–446, doi:10.1002/2014EO480001.

Marti, L., A. Rezaei-Zare, and D. Boteler (2014a), Calculation of induced electric field during a geomagnetic storm using recursive convolution, *IEEE Trans. Power Delivery*, *29*(2), 802–807.

Marti, L., C. Yiu, A. Rezaei-Zare, and D. Boteler (2014b), Simulation of geomagnetically induced currents with piecewise layered-Earth models, *IEEE Trans. Power Delivery*, *29*, 1186–1193, doi:10.1109/TPWRD.2014.2317851.

McKay, A. J., K. A. Whaler, and Geophys. J. Int. (2006), The electric field in northern England and southern Scotland: implications for geomagnetically induced currents, *167*, 613–625, doi:10.1111/j.1365-246X.2006.03128.x.

Meqbel, N. M., G. D. Egbert, P. E. Wannamaker, A. Kelbert, and A. Schultz (2014), Deep electrical resistivity structure of the northwestern U.S. derived from 3D inversion of USArray magnetotelluric data, *Earth Planet. Sci. Lett.*, *402*, 290–304, doi:10.1016/j.epsl.2013.12.026.

North American Electric Reliability Corporation (NERC) (1990), March 13, 1989 Geomagnetic Disturbance Report, pp. 36–60.

North American Electric Reliability Corporation (NERC) (2012), Special reliability assessment interim report: Effects of geomagnetic disturbances on the bulk power system. [Available at: https://www/free.com/Public%20Awareness/Lists/Announcements/Atttachments/105/GMD%20Interim\%20Report.pdf, accessed on 7 August 2013.]

National Science and Technology Council (2015), *National Space Weather Action Plan*, pp. 1–38, Executive Office, Natl. Sci. Tech. Council, Washington, D. C.

Piccinelli, R., and E. Krausmann (2014), *Space Weather and Power Grids—A Vulnerability Assessment*, pp. 1–53, European Union, Luxembourg.

Pulkkinen, A., R. Pirjola, and A. Viljanen (2007), Determination of ground conductivity and system parameters for optimal modeling of geomagnetically induced current flow in technological systems, *Earth Planets Space*, *59*, 999–1006.

Pulkkinen, A., R. Kataoka, S. Watari, and M. Ichiki (2010), Modeling geomagnetically induced currents in Hokkaido, Japan, *Adv. Space Res.*, *46*(9), 1087–1093, doi:10.1016/j.asr.2010.05.024.

Pulkkinen, A., E. Bernabeu, J. Eichner, C. Beggan, and A. W. P. Thomson (2012), Generation of 100-year geomagnetically induced current scenarios, *Space Weather*, *10*, 1–19, doi:10.1029/2011SW000750.

Pulkkinen, A., et al. (2017), Geomagnetically induced currents: Science, engineering and applications readiness, *Space Weather*, *15*, doi:10.1002/2016SW001501.

Samuelsson, O. (2013), *Geomagnetic Disturbances and Their Impact on Power Systems*, pp. 1–18, Ind. Elec. Eng. Auto., Lund Univ., Lund, Sweden.

Schultz, A., G. D. Egbert, A. Kelbert, T. Peery, V. Clote, and B. Fry (2006-2018), Staff of the National Geoelectromagnetic Facility, and their contractors, *USArray TA Magnetotelluric Transfer Functions*, doi:10.17611/DP/EMTF/USARRAY/TA.

Simpson, F., and K. Bahr (2005), *Practical Magnetotellurics*, 1–254 pp., Cambridge Univ. Press, Cambridge, U. K.

Sims, W. E., F. X. Bostick, and H. W. Smith (1971), The estimation of magnetotelluric impedance tensor elements from measured data, *Geophysics*, *36*(5), 938–942.

Siripunvaraporn, W., G. D. Egbert, Y. Lenbury, and M. Uyeshima (2005), Three-dimensional magnetotelluric inversion: Data-space method, *Phys. Earth Planet. Inter.*, *150*(1–3), 3–14.

Smirnov, M. Y., and G. D. Egbert (2012), Robust principal component analysis of electromagnetic arrays with missing data, *Geophys. J. Int.*, *190*, 1423–1438, doi:10.1111/j.1365-246X.2012.05569.x.

Thomson, A. W. P., A. J. McKay, and A. Viljanen (2009), A review of progress in modelling of induced geoelectric and geomagnetic fields with special regard to induced currents, *Acta Geophys.*, *57*, 209–219.

Torta, J. M., S. Marsal, and M. Quintana (2014), Assessing the hazard from geomagnetically induced currents to the entire high-voltage power network in Spain, *Earth Planets Space*, *66*, 87, doi:10.1186/1880-5981-66-87.

Viljanen, A., A. Pulkkinen, R. Pirjola, K. Pajunpaa, P. Posio, and A. Koistinen (2006), Recordings of geomagnetically induced currents and a nowcasting service of the Finnish natural gas pipeline system, *Space Weather*, *4*, 1–9, doi:10.1029/2006SW000234.

Viljanen, A., R. Pirjola, E. Prácser, S. Ahmadzai, and V. Singh (2013), Geomagnetically induced currents in Europe: Characteristics based on a local power grid model, *Space Weather*, *11*, 575–584.

Vozoff, K (1972), The magnetotelluric method in the exploration of sedimentary basins, *Geophysics*, *1*, 98–141.

Wei, L. H., N. Homeier, and J. L. Gannon (2013), Surface electric fields for North America during historical geomagnetic storms, *Space Weather*, *11*, 451–462, doi:10.1002/swe.20073.

Weidelt, P. (1972), The inverse problem of geomagnetic induction, *Z. Geophys.*, *38*, 257–289.

Weidelt, P., and A. D. Chave (2012), The magnetotelluric response function, in *The Magnetotelluric Method*, edited by A. D. Chave and A. G. Jones, pp. 122–164, Cambridge Univ. Press, Cambridge, U. K.

Weigel, R. S. (2017), A comparison of methods for estimating the geoelectric field, *Space Weather*, *15*(2), 430–440, doi:10.1002/2016SW001504.

Yang, B., G. D. Egbert, A. Kelbert, and N. M. Meqbel (2015), Three-dimensional electrical resistivity of the north-central USA from EarthScope long period magnetotelluric data, *Earth Planet. Sci. Lett.*, *422*, 87–93.